IEEE Photonics Journal
An IEEE Photonics Society Publication

Open Access

Characteristics and Performance of Image Sensor Communication

Volume 9, Number 2, April 2017

Wei Huang
Zhengyuan Xu, ***Senior Member, IEEE***

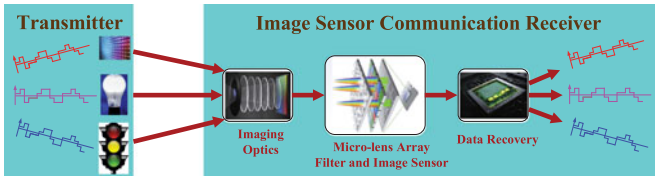

DOI: 10.1109/JPHOT.2017.2681660
1943-0655

IEEE photonics SOCIETY

IEEE

Characteristics and Performance of Image Sensor Communication

Wei Huang[1] **and Zhengyuan Xu,**[1,2] ***Senior Member, IEEE***

[1]Key Laboratory of Wireless-Optical Communications, Chinese Academy of Sciences, School of Information Science and Technology, University of Science and Technology of China, Hefei, Anhui 230027, China
[2]Shenzhen Graduate School, Tsinghua University, Shenzhen 518055, China

DOI:10.1109/JPHOT.2017.2681660

Manuscript received February 8, 2017; revised March 5, 2017; accepted March 9, 2017. Date of publication March 14, 2017; date of current version April 5, 2017. This work was supported in part by the National Key Basic Research Program of China under Grant 2013CB329201, in part by the Key Program of the National Natural Science Foundation of China under Grant 61631018, in part by the Key Research Program of Frontier Sciences of the Chinese Academy of Sciences under Grant QYZDY-SSW-JSC003, in part by the Key Project in Science and Technology of Guangdong Province under Grant 2014B010119001, and in part by the Shenzhen Peacock Plan under Grant 1108170036003286.
Corresponding author: Z. Xu (e-mail: xuzy@ustc.edu.cn).

Abstract: A complementary metal-oxide semiconductor (CMOS) image sensor can be used for communication, in addition to imaging. This paper investigates noise characteristics and system performance for CMOS image sensor communication. Different signal-dependent and independent noise sources are categorized and comprehensively analyzed in conjunction with sensor measurements. Accordingly, a unified channel model in the pixel-matched case is proposed, and the communication signal-to-noise ratio is defined and demonstrated in different parameter settings. Moreover, the channel capacity with mixed noise and bounded input is derived and is proven to be achievable by a discrete input distribution of finite number of probability mass points. Simulation shows that capacity of more than 7 b/s/Hz per pixel or 8–10 b/s/Hz per block of multiple pixels is achievable.

Index Terms: Image sensor communication, mixed signal-dependent Gaussian noise, capacity.

I. Introduction

Most modern personal mobile devices or high-end professional camcorders use complementary metal-oxide semiconductor (CMOS) image sensors due to their excellent performance and cost tradeoffs. According to the Grand View Research report about the image sensor market [1], CMOS shipments amounted to 3.6 billion units or 97% market share by 2015, compared to charge coupled device (CCD) shipments.

Recently, optical camera communication (OCC) or image sensor communication (ISC) emerges as a new form of visible light communication (VLC). It employs a CMOS image sensor assembled in consumer electronics, such as smartphone and iPad, as an alternative receiver to the traditional photodiode (PD) or avalanche photodiode (APD) receiver [2], [3]. The sensor contains millions of pixels. Aided by a micro front lens, it can easily classify multiple spatially separated light sources. Meanwhile, its multi-color filter layout, such as the Bayer-pattern color filter or Foveon X3 color filter, can separate the blended multi-color transmissions. These appealing features in the spatial and color dimensions help support a huge number of parallel transmissions. The ISC can be applied in intelligent transport system (ITS) [4], near field communication (NFC) [5], and indoor positioning

[6]. A working group within the IEEE is dedicated to revision of formerly established IEEE 802.15.7 VLC standard, and incorporating ISC physical layer functionalities and MAC modifications [7], [8].

There have been various research works on the ISC modulation schemes [3], synchronization [9], and system implementation [10], but some fundamental questions still exist in ISC, such as the noise characteristics and system performance. Generally, the sensor generates random output current due to the quantum nature of the device. The inherent shot noise is typically modeled by Poisson statistics and becomes signal dependent. As the number of impinging photons increases, the shot noise process can be well approximated by signal dependent Gaussian statistics. Together with thermal noise, the ISC channel can be described by an additive white Gaussian noise (AWGN) model [11]. On the other hand, an optical communication system is vulnerable to outside optical noise. It has been shown that the solar background light in an outdoor ISC system of large field-of-view (FOV) can easily overwhelm the desired signal even if an optical bandpass filter is used [12]. Among different noise sources, their roles in determining system performance remain open and require thorough analytical investigation.

In this paper, we focus on the ISC noise characteristics and system performance. Strongly motivated by the pioneering experimental measurement and data fitting results [11], we analyze the noise from sensor's schematic circuit to better reflect the internal physical nature. Due to the sensor complex structure, we also examine many other noise sources in a typical active pixel sensor (APS) during each phase of its operation. They include photo response non-uniformity (PRNU) [13], photo shot noise [14], dark current shot noise [15], source follower noise [16], sense node reset noise [17], and quantization noise [16]. We show by simulation and experimental measurement that the mixture of different noise sources still follows a Gaussian distribution whose variance depends on individual noise characteristics and input signal. The dark current fixed-pattern noise (FPN) [18] and offset FPN [13] are not taken into account, considering their time-invariant and signal-independent characteristics.

Those noises play different roles in the ISC system performance. They in turn depend on sensor's key specifications and communication settings. Based on the noise model, we propose a communication signal-to-noise ratio (SNR) model in the ideal pixel-matched channel unifying different contributions. From the model, the effects of photocurrent, integration time and block size are numerically demonstrated. Again from the model, we further derive the capacity for this intensity constrained channel. Moreover, following similar arguments in existing capacity study on optical channels [19]–[22], we prove that the capacity of such mixed signal-dependent Gaussian noise (M-SDGN) channel is achieved by a discrete input distribution of finite number of probability mass points. We apply the search algorithm in [21] to find the capacity-achieving probability measure and the maximum mutual information.

The paper is organized as follows. The noise characteristics in the CMOS image sensor are analyzed in Section II. Section III first gives definition of the communication system SNR, and then presents a unified ISC channel model in the pixel-matched case. Moreover, the capacity under intensity constraints is derived. The simulation and experimental results for noise characteristics, SNR and capacity are provided in Section IV. Finally, Section V concludes this work.

II. Characteristics of Various Noises in a CMOS Image Sensor

A CMOS image sensor suffers from several fundamental and technology related noises, including ambient noise, temporal noise and FPN [13]. Temporal noise, which is defined as the temporal variation of pixel output values under uniform illumination due to the device noise, is the dominant noise in the sensor. Sources of temporal noise include photodetector shot noise, pixel reset circuit noise, readout circuit thermal and flicker noise, and quantization noise. FPN captures the pixel-to-pixel output variation under uniform illumination due to device and interconnect mismatches across the sensor array.

In this section, we analyze the sources of noise in a typical 5-T APS during each phase of its operation, including photon to charge operation, charge to voltage operation, and voltage to digital numbers operation [16], based on the photosensor model in Fig. 1. To simplify the analy-

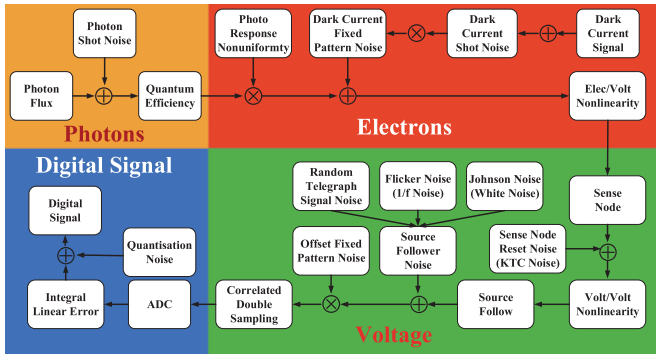

Fig. 1. Diagram of the photosensor model.

sis, the electrons-to-voltage, voltage-to-voltage, analog-to-digital converter non-linearities are not considered in this paper.

2.1 From Photon to Charge

The photon capturing process has an uncertainty that arises from random fluctuations of the sensor output when photons are collected by the photodiode. Such uncertainty leads to *photon shot noise* and can be described by the Poisson process. In the case of a high illumination level, the Poisson distribution can be approximated by a Gaussian distribution [23]. Denote the average number of photons I_{photon} collected by a single pixel during unit integration time as

$$I_{photon} = \text{round}\left(\frac{I_{irrad} \cdot P_A}{E_p}\right) \tag{1}$$

where I_{irrad} is sensor's irradiance with unit of $[W/m^2]$, P_A is the pixel sensor area, $E_p = \frac{h \cdot c}{\lambda}$ is the energy of a single photon at wavelength λ, h is Planck's constant, and c is light speed. The photon shot noise corresponding to sensor pixels can be modeled as a Poisson process $\mathcal{P}$ with mean λ_{ph} as $\mathcal{P}(\lambda_{ph})$, where $\lambda_{ph} = I_{photon}$. Then the collected photons during exposure time t_{int}, including the shot noise, are converted to electrons I_{e^-} as

$$I_{e^-} = I_{photon} \cdot QE \cdot t_{int} = I_{ph} \cdot t_{int} \tag{2}$$

where QE is the *quantum efficiency* [e^-/incident photon] for the given wavelength, indicating the ability of a semiconductor to produce electrons from incident photons.

The PRNU, also called *gain FPN*, captures the spatial variation in pixel output under uniform illumination. It is mainly due to the variation in substrate material characteristics during the fabrication of the photodiodes. Moreover, it is signal-dependent and has a fixed pattern (time-invariant) [13], [16]. The PRNU I_{PRNU,e^-} normalized by I_{e^-} can be modeled by a Gaussian distribution with zero mean and standard deviation σ_{PRNU} (also called PRNU factor value) as $\mathcal{N}(0, \sigma^2_{PRNU})$. It is additive to the signal electrons I_{e^-} to generate the total light signal output I_{light,e^-}.

The thermally generated electrons discharge each pixel, equivalent as that photons hit the pixel. Together with the surface defects and imperfections of the semiconductor manufacturing process, *dark current* is inevitable. When pixel exposure begins, a dark current is generated even if there is no light. The average dark current I_{dc} [e^-/s/pixel] can be characterized by

$$I_{dc} = P_A I_{FM} T^{3/2} \exp\left(\frac{-E_{gap}}{2k_B T}\right) \tag{3}$$

where I_{FM} $[nA/cm^2]$ is the dark current figure-of-merit at 300K, T $[K]$ is the temperature in Kelvin, k_B is the Boltzman's constant, E_{gap} $[eV]$ is the band gap energy of the semiconductor which varies with temperature. The longer the integration time t_{int}, the stronger the dark signal S_{dark,e^-} (number

of electrons per pixel) modeled as

$$S_{dark,e^-} = I_{dc} \cdot t_{int}. \tag{4}$$

It varies from pixel to pixel and doubles with every $6 \sim 8^o$ C increase of temperature when measured at the room temperature $+25^o$ C. However, since the electrons are generated randomly, the dark signal is a subject of a *dark current shot noise*. Similar to the photon shot noise, the dark current shot noise $I_{dark,shot,e^-}$ is due to the random arrival of the generated electrons and described by a Poisson process $\mathcal{P}(\lambda_{dark,e^-})$ with parameter S_{dark,e^-}.

In a practical sensor, pixels can't be uniformly manufactured from perfectly pure materials. There will always be the variations in the photodetector area which provide a mechanism for thermally-excited carriers to move between the valence and conduction bands. Consequently, the average dark signal is not uniform but has a spatially-random and fixed pattern noise structure, which is called *dark current FPN*. In this paper, we use Log-Normal distribution to model the dark current FPN I_{dark,FPN,e^-} in the case of short integration time [16]. Normalized by the dark current shot noise $I_{dark,shot,e^-}$, the dark current FPN follows this distribution $\ln\mathcal{N}(0, \sigma^2_{dark,FPN,e^-})$, where

$$\sigma_{dark,FPN,e^-} = \xi_{dark,FPN} \cdot I_{dc} \cdot t_{int}, \tag{5}$$

and $\xi_{dark,FPN}$ is the average dark current FPN factor typically taking a value of $0.1 \sim 0.4$ for most sensors. The dark signal I_{dark,e^-} is a superposition of the dark current shot noise $I_{dark,shot,e^-}$ and dark current PFN.

In most commercial CMOS sensors, the source follower noise I_{SF,e^-} is significant and should be included in a photosensor model. It consists of *white noise* (or Johnson noise), *flicker noise* ($1/f$ noise), and *random telegraph noise* (RTN) [16]. It has a Gaussian distribution with zero mean and standard deviation in [e^- *rms*] approximated as

$$\sigma_{SF} \approx \frac{\sqrt{\sum_{f=1}^{f_{clock}} S_{SF}(f) \cdot H_{CDS}(f)}}{A_{SN} \cdot A_{SF}(1 - \exp[-t_s/\tau_D])} \tag{6}$$

where $S_{SF}(f)$ is the power spectrum of the noise, $H_{CDS}(f)$ is the correlated double sampling (CDS) transfer function, f_{clock} is the readout clock frequency, A_{SN} [V/e^-] is a sense node conversion gain, A_{SF} is a source follower gain, t_s is the CDS sample-to-sampling time, and τ_D is the CDS dominant time constant usually related to t_s as $\tau_D = 0.5t_s$.

2.2 From Charge to Voltage

After the charge is generated, electron-voltage conversion is applied to convert the electrons to voltage by multiplying the sense node conversion gain G_{SN}. Specifically, the charge-voltage conversion uses the sense node gain A_{SN} as a parameter in the range of $1\ \mu V/e^- \sim 5\ \mu V/e^-$ to convert the electrons to voltage as follows:

$$V_{SN,V} = V_{\mathrm{ref}} - I_{total,e^-} \cdot A_{SN} \tag{7}$$

where $V_{SN,V}$ is the sense node voltage, V_{ref} is the reference voltage, and I_{total,e^-} is the total number of electrons. I_{total,e^-} is a superimposed contribution from the light signal I_{light,e^-}, dark signal I_{dark,e^-}, and source follower noise I_{SF,e^-}, and further truncated to the *full well* (the maximum number of electrons in the pixel) and rounded as follows:

$$I_{total,e^-} = round(I_{light,e^-} + I_{dark,e^-} + I_{SF,e^-}). \tag{8}$$

The reference voltage V_{ref} in (7) is applied to the sense node capacitor prior to measuring each pixel's charge. Due to thermal variations in the channel resistance of the MOSFET reset transistor, *reset noise* $V_{SN,reset,V}$ is generated at the sense node by an uncertainty in the reference voltage level. Its distribution depends on sensor's architecture and the reset technique. Here, Log-Normal

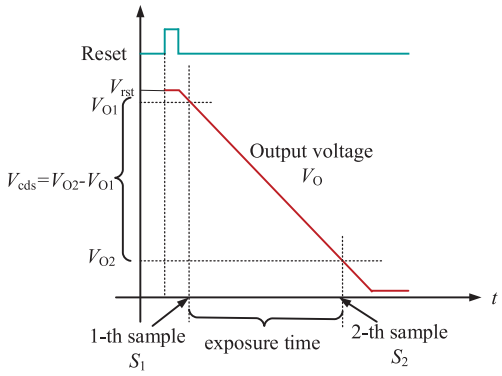

Fig. 2. Correlated double sampling (CDS) process for a pixel.

distribution $\ln\mathcal{N}(0, \sigma^2_{reset})$ is used to model the reset noise for soft-reset techniques, where

$$\sigma_{reset} = \sqrt{\frac{k_B T}{C_{SN}}} \tag{9}$$

where C_{SN} is the sense node capacitance $[F]$. Therefore, the reference voltage V_{ref} is a random variable consisting of a constant voltage level and the reset noise.

Afterwards, the sense node voltage is multiplied by the source follower gain $A_{SF}[V/V]$, yielding the source follower voltage $V_{SF,V}$ as

$$V_{SF,V} = V_{SN,V} \cdot A_{SF}. \tag{10}$$

In particular, for a CMOS image sensor, pixels in the same column of the photosensor share a common column amplifier. Differences in the gain and offset of these column amplifiers contribute to a column-wise *offset FPN*. The offset FPN appears as "stripes" in the received image, which will significantly degrade the system performance but can be removed by the noise reduction circuits in a nowadays image sensor.

In most high-performance image sensors, the noise reduction circuits such as *correlated double sampling* (CDS) are employed to eliminate or reduce the FPN and reset noise, as illustrated in Fig. 2. The CDS circuits are located in each column and usually consist of two sample-and-hold circuits. During the pixel read-out cycle, two samples are taken: the first when the pixel is in the reset state and the second when the charge has been transferred to the read-out node [13]. During the reset cycle, the photodiode capacitor is charged to a reset voltage. The reset voltage is read by the first sample-and-hold in a CDS circuit. Then, the exposure begins: the photodiode capacitor is discharged during an integration time at a rate proportional to the incident illumination. This voltage is then read by the second sample-and-hold of the CDS. The CDS circuit subtracts the signal pixel value from the reset value.

Although the dark current FPN and reset noise can be removed by CDS in CCD sensors, they are difficult to remove in CMOS sensors even after application of CDS. These noises can be suppressed by CDS but the process leads to increased read noise power.

2.3 From Voltage to Digital Numbers

After the electrons have been converted to a voltage signal followed by source follower amplification, an analog-to-digital convertor (ADC) transforms the voltage signal into a discrete code. An N-bit ADC produces $N_{\max} = 2^N$ possible output codes. The voltage difference between two neighboring codes is $V_{ADC,ref}/2^N$, $V_{ADC,ref}$ is the maximum voltage. The ADC resolution indicates the number

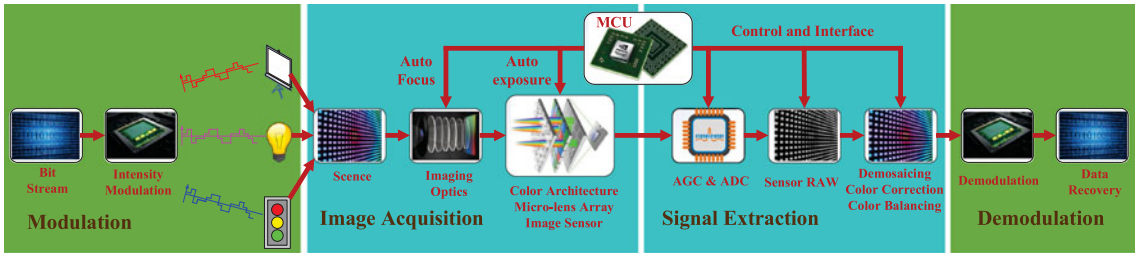

Fig. 3. ISC system block diagram.

of discrete values that can be produced over the range of analog value, as

$$K_{ADC} = \frac{V_{ADC,ref} - V_{\min}}{N_{\max}} \tag{11}$$

where $V_{\min}$ is the minimum quantifiable voltage. The output of an ADC can be expressed as

$$ADC_{code} = round\left(\frac{V_{SF,V} - V_{\min}}{K_{ADC}}\right) \tag{12}$$

where $V_{SF,V}$ is the total voltage signal accumulated by the end of the integration time and conversion, as in (10). After finite precision quantization, a quantization error is inevitable. The quantization noise is generally assumed to be a uniform random variable. Its standard deviation has a form

$$\sigma_{ADC} = \sqrt{\frac{q_{ADC}^2}{12}} \tag{13}$$

where $q_{ADC} = 2^{-b}$ is the quantizing step of the ADC, and $(b+1)$ is the ADC bit.

III. ISC System Performance and Capacity

3.1 System Model and SNR With M-SDGN

Different from the noise and SNR defined in image processing, we analyze the noise from the communication perspective under high illumination. Essentially, ISC is an intensity modulate-direct detection (IM-DD) system. A typical transceiver diagram is shown in Fig. 3. The input signal is proportional to the light intensity and is therefore nonnegative. As a power detecting unit, each pixel responds to the instantaneous field and its output appears as a shot noise process whose count rate is proportional to the instantaneous received power. The received signal is corrupted by different noises. In addition to background radiation, the number of electrons generated by each pixel is a Poisson random process with a rate proportional to the input signal power. This process generates signal dependent noise. It is noteworthy that other FPNs except PRNU are not damage factors for a fixed single pixel or pixel-group based receiver, because these FPNs are time-invariant and signal-independent. Moreover, the signal is also impaired by read noise, a combination of the remained noise generated by the follow-up ADC circuitry.

In the pixel-matched case, we only consider aforementioned front-end noise sources, but ignore interference and the alignment error. Moreover, the channel gain h is set to 1 without loss of generality, since the constant h only represents link and optoelectronic conversion losses [24]. Then, the converted electrical signal from a pixel readout circuit can be expressed as

$$Y = X + XZ_2 + \sqrt{X}Z_1 + Z_0. \tag{14}$$

Here, $X = I_{ph}t_{int}$ is the desired electrical signal and is proportional to the channel input. There exist three noise terms. $Z_0 \sim \mathcal{N}_{\mathbb{R}}(0, \sigma^2)$ is the signal-independent Gaussian noise, including shot noise contributed by background light and dark current, background light induced PRNU, and the read

noise. The parameter

$$\sigma^2 = q(I_{dc} + I_{back})t_{int} + \sigma^2_{PRNU}(I_{back}t_{int})^2 + q^2(\sigma^2_{reset} + \sigma^2_{SF} + \sigma^2_{ADC}) \tag{15}$$

describes the strength of the signal-independent noise, where I_{back} is the current induced by background radiation. The second and third terms in the model are signal-dependent noise terms with variances $\varsigma_2^2\sigma^2X^2$ and $\varsigma_1^2\sigma^2X$ respectively. Parameters ς_1^2 and ς_2^2 are the ratios of the variances of Z_1 and Z_2 to the variance of Z_0 respectively. $Z_1 \sim \mathcal{N}_{\mathbb{R}}(0, \varsigma_1^2\sigma^2)$ is due to input-signal induced shot noise, and $Z_2 \sim \mathcal{N}_{\mathbb{R}}(0, \varsigma_2^2\sigma^2)$ comes from PRNU. Assume Z_2 and Z_1 are independent of Z_0.

The proposed channel model follows closely the received signal model in [25] as below, in the presence of the signal-dependent film-grain noise or the photoelectric shot noise

$$Y = hX + kf(X)Z_1 + Z_0 \tag{16}$$

where Z_1 and Z_0 are independent random noises, $f(X)$ is some function of the signal, h and k are scalar constants. The commonly used model in image processing obeys by a specific form of $f(X) = X^p$ when the observed quantity is photographic density [25].

Motivated by the above, the signal-dependent noise channel can be rewritten as a general form

$$Y = hX + \sum_{n=1}^{N} X^{p_n}k_nZ_n + Z_0 \tag{17}$$

where $p_n \geq 0$ is the exponential index which can be arranged in a column vector $\boldsymbol{p} = [p_1, \ldots, p_N]^T$ for convenience, similarly for the scale vector $\boldsymbol{k} = [k_1, \ldots, k_N]^T$ and noise vector $\boldsymbol{Z} = [Z_1, \ldots, Z_N]^T$. Their dimension N depends on the number of noise sources. Specially, when $h = 1$ and $N = 0$, the channel model degrades to the most common signal-independent Gaussian noise channel. When $h = 1$, $N = 1$, $k = 1$, $p_1 = \frac{1}{2}$, it represents the improved free-space intensity channel as in [26]. The proposed M-SDGN channel in (14) is a special case of when $h = 1$, $N = 2$, $\boldsymbol{k} = [1, 1]^T$, $\boldsymbol{Z} = [Z_1, Z_2]^T$, $\boldsymbol{p} = [\frac{1}{2}, 1]^T$.

The conditional probability density function (PDF) of the channel output is given by

$$f_{Y|X}(y|x) = \frac{1}{\sqrt{2\pi\sigma^2(1 + \varsigma_2^2x^2 + \varsigma_1^2x)}} e^{-\frac{(y-x)^2}{2\sigma^2(1+\varsigma_2^2x^2+\varsigma_1^2x)}} \qquad x \in \mathbb{R}^+, y \in \mathbb{R}. \tag{18}$$

Due to safety and practical considerations, the input signal has a peak intensity (amplitude) and nonnegative constraint $P_r[0 \leq X \leq A] = 1$ and an average-intensity constraint $E[X] \leq P$. Denote average-to-peak-power ratio (APPR) by $\rho \triangleq P/A$. Note that the input signal is proportional to the light intensity. Thus, the power constraint is imposed on the signal itself, instead of its square as in RF communication. Then, we quantify the received SNR of the ISC system as

$$\text{SNR} = \frac{E\{X^2\}}{\sigma^2E(1 + \varsigma_2^2X^2 + \varsigma_1^2X)}. \tag{19}$$

It is a function of photocurrent, pixel area, integration time, and so on. In addition, one can leverage the spatial diversity to improve SNR by grouping multiple pixels into a block to map one transmitter. Assuming B pixels in the block whose ith pixel output is Y_i, the average output gray value for this block is $Y = \frac{1}{B}\sum_{i=1}^{B} Y_i$. By grouping multiple pixels as a block receiver, the noise will be reduced by spatial averaging. Thus, SNR also depends on the block size.

3.2 Channel Capacity With Bounded-Input and M-SDGN

The channel capacity can better reflect the physical channel properties and ultimate communication performance. In the following, we will focus on this Gaussian channel with M-SDGN and derive the capacity with bounded input.

The channel model (14) is a special case of the general signal-dependent channel model (17). Unfortunately, the capacity of the M-SDGN channel is unknown, and it is difficult to apply the sphere packing method or the dual expression approach. However, following similar arguments as in [19]–[22], we can prove that the mutual information function is a concave, continuous, and weakly differentiable function over a compact and convex space of distribution, and the capacity of this M-SDGN channel is achieved by a discrete input distribution.

For the channel described by (14), we assume the input signal has an amplitude constraint $X \in [0, A]$. Let $\mathcal{F}_X$ denote the convex space of cumulative distribution functions F_X. Thus $F_X \in \mathcal{F}_X$ implies that $F_X(x) = 0$ for all $x < 0$ and $F_X(x) = 1$ for all $x \geq A$. The existence of $f_Y(y; F_X)$ is guaranteed by the boundedness and integrability of the conditional $f_{Y|X}(y|x)$, which can be bounded by

$$q(y) \leq f_{Y|X}(y|x) \leq Q(y) \tag{20}$$

where

$$q(y) = \min_{x\in[0,A]} f_{Y|X}(y|x) = k_1 e^{-k_2(y-x_0)^2} \tag{21}$$

with $x_0 = \arg\min_{x\in[0,A]} f_{Y|X}(y|x)$, and

$$Q(y) = \max_{x\in[0,A]} k_3 e^{\frac{-(y-x)^2}{2\pi\sigma^2(1+\varsigma_2^2x^2+\varsigma_1^2x)}} \tag{22}$$

with $k_3 \triangleq \max_{x\in[0,A]} \frac{1}{\sqrt{2\pi\sigma^2(1+\varsigma_2^2x^2+\varsigma_1^2x)}} < \infty$. As a result, the probability density function $f_Y(y; F_X)$ can be bounded as well:

$$\gamma(y) \leq f_Y(y; F_X) \leq \Gamma(y) \tag{23}$$

where

$$\gamma(y) = q(y), \quad \text{and} \quad \Gamma(y) = Q(y). \tag{24}$$

For a given distribution F_X on the channel input X, the average mutual information between X and Y and the output entropy will be denoted by $I_{F_X}(X; Y)$ and $H_{F_X}(Y)$, respectively. The conditional entropy $H_{F_X}(Y|X)$ is given by

$$\begin{aligned} H_{F_X}(Y|X) &= \int_0^A H(Y|X = x)dF_X(x) \\ &= \int_0^A \frac{1}{2}\log\left(2\pi e\sigma^2(1 + \varsigma_2^2x^2 + \varsigma_1^2x)\right)dF_X(x) \\ &= \frac{1}{2}\log(2\pi e\sigma^2) + \frac{1}{2}E\left[\log(1 + \varsigma_2^2x^2 + \varsigma_1^2x)\right]. \end{aligned} \tag{25}$$

Note that the function $(1 + \varsigma_2^2x^2 + \varsigma_1^2x)$ is continuous and bounded, hence the expectation in (25) exists. Thus, the average mutual information $I_{F_X}(X; Y)$ can be expressed as

$$I_{F_X}(X; Y) = H_{F_X}(Y) - D - \frac{1}{2}E\left[\log(1 + \varsigma_2^2x^2 + \varsigma_1^2x)\right] \tag{26}$$

where $D = \frac{1}{2}\log(2\pi e\sigma^2)$.

Moreover, we define the mutual information density $i_{F_X}(x)$ and entropy density $h_{F_X}(x)$ as

$$i_{F_X}(x) \triangleq \int_{-\infty}^{\infty} f_{Y|X}(y|x)\log\frac{f_{Y|X}(y|x)}{f_Y(y;F_X)}dy \tag{27}$$

$$h_{F_X}(x) \triangleq -\int_{-\infty}^{\infty} f_{Y|X}(y|x)\log f_Y(y;F_X)dy. \tag{28}$$

Thus, the following equation holds:

$$i_{F_X}(x) = h_{F_X}(x) - D - \frac{1}{2}\log(1+\varsigma_2^2x^2+\varsigma_1^2x). \tag{29}$$

The channel capacity $\mathcal{C}$ is defined as the maximum of the mutual information over the space of distribution functions $\mathcal{F}_X$, given by

$$\mathcal{C} = \max_{F_X\in\mathcal{F}_X} I_{F_X}(X;Y). \tag{30}$$

In the following, we will present the results on the capacity maximization problem of this M-SDGN channel with bounded input. The results show that the optimal distribution maximizing the mutual information is discrete and non-uniform. To accomplish this, we state the following theorems for the proof of propositions later on [27].

Dominated Convergence Theorem: Let $(f_n)_{n\in\mathbb{N}}$ be a sequence of integrable function which converges almost everywhere to a real valued measurable function f. If there exists an integrable function g such that $|f_n| \le g$ for all n, then f is integrable and $\lim_n \int f_n d\mu = \int f d\mu$.

Morera's Theorem: Let function $f : \mathbb{C} \to \mathbb{C}$ be continuous in a connected open set $\mathcal{D}$. If $\oint_\gamma f(z)dz = 0$ for every closed curve γ in $\mathcal{D}$, then f is an analytic function in $\mathcal{D}$.

Identity Theorem: If two functions, analytic in some region of the complex plane, agree on an infinite set of points in that region and the set of points has a limit point in that region, then the functions are equal in that region.

Remark 1: Let f: $\mathbb{R} \to \mathbb{R}$ be a positive-value and bounded function, i.e., $0 \le f(y) \le c \le \infty$ for any $y \in \mathbb{R}$ and some positive constant c [22]. Then, the following inequality holds:

$$|\log(f(y))| \le -\log(f(y)) + 2|\log c|. \tag{31}$$

Lemma 3.1: $\mathcal{F}_X$ is compact in the Levy metric topology and convex.

Proof: See [28]. ■

Proposition 3.1: The mutual information function $I_{F_X}(X;Y)$ is a continuous and concave function of the distribution F_X and, moreover, a weakly differentiable function over $\mathcal{F}_X$.

Proof: See Appendix A. ■

Proposition 3.2: The capacity-achieving distribution is discrete with finite number of mass points.

Proof: See Appendix B. ■

Theorem 1: Capacity $\mathcal{C}$ is achieved by a random input, denoted by X_0 with probability distribution function $F_0 \in \mathcal{F}_X$, i,e.,

$$\mathcal{C} = \max_{F_X\in\mathcal{F}_X} I_{F_X}(X;Y) = I_{F_0}(X;Y) \tag{32}$$

for some $F_0 \in \mathcal{F}_X$. A sufficient and necessary condition for F_0 to achieve capacity is

$$i_{F_0}(x) \le I_{F_0}(X;Y), \quad \forall x \in [0, A]. \tag{33}$$

Furthermore, this distribution is discrete and consists of finite number of mass points if some technical conditions on $(1+\varsigma_2^2x^2+\varsigma_1^2x)$ hold.

Proof: Based on Lemma 3.1 and Proposition 3.1, it has been proven that $\mathcal{F}_X$ is convex and compact in some topology, and mutual information $I_{F_X}(X;Y) : \mathcal{F}_X \to \mathbb{R}$ is continuous, concave and weakly differentiable over the input distribution. Thus, invoking the KKT Theorem results in sufficient and necessary conditions for the optimal input distribution, there is an unique optimal input distribution $F_0 \in \mathcal{F}_X$, that achieves the maximum mutual information. Finally, according to

TABLE I
Parameters of the CMOS Sensor Provided by Manufacturer

Manufacture process	CMOS	Model number	OV4688
Pixel size	2 μm $\times$ 2 μm	Number of pixels	672 $\times$ 380
Output formats	10-bit RAW RGB	Frame rate	330 fps
Binning	4 $\times$ 4	Dark current	4 mV/sec 60^{o} C junction temperature

TABLE II
Image Sensor Key Specifications

Manufacture process	CMOS	PRNU factor	0.6 % $\sim$ 1 %
Pixel size	3.75 μm $\times$ 3.75 μm	Dark current FPN factor	1%
Number of pixels	1080 $\times$ 720	Column offset FPN factor	0.1%
Wavelength λ	550 nm	Dark current figure of merit	1.00 nA/cm^2
Fill factor	55%	Sense node gain	5.00 μV/e$^-$
Quantum efficiency	65 %	Read nose σ_{read}	30 e^-
Full well	60000 e^-	ADC bit	12 bit

Proposition 3.2, it is demonstrated that the capacity-achieving distribution is discrete with finite number of mass points. ■

Above theorem ensures a finite number of mass points for finite A and P. We can use the search algorithm as in [21] to find the optimal input distribution and the corresponding maximum mutual information for such constrained channel.

IV. Numerical Results

In this section, we first investigate the CMOS image sensor noise properties according to our simulation and sensor measurements. Since not all the parameters of the image sensor are provided the manufacturer, for example the nonlinearity factors, the PRNU factor and the sense node gain. However, we use the typical specifications of an image sensor as the unknown key parameters, and adjust the parameters in confidence interval to make the simulation results and measurement results coincide. Table I lists the key specifications of the CMOS image sensor used in the experiment, while Table I and Table II list the key specifications of the image sensor used in computer simulations. Since the photocurrent I_{ph} is not directly measurable, we obtain its value from incident light intensity and subsequently investigate characteristics of the received noise by simulation, and the communication SNR with different parameters by simulation. Finally, we present the ISC channel capacity under different constraints.

4.1 Sensor Noise Characteristics

In order to verify the Gaussian noise distribution and signal dependence, we collect the gray values of an arbitrarily chosen pixel in both simulated and measured RAW images over 50000 frames

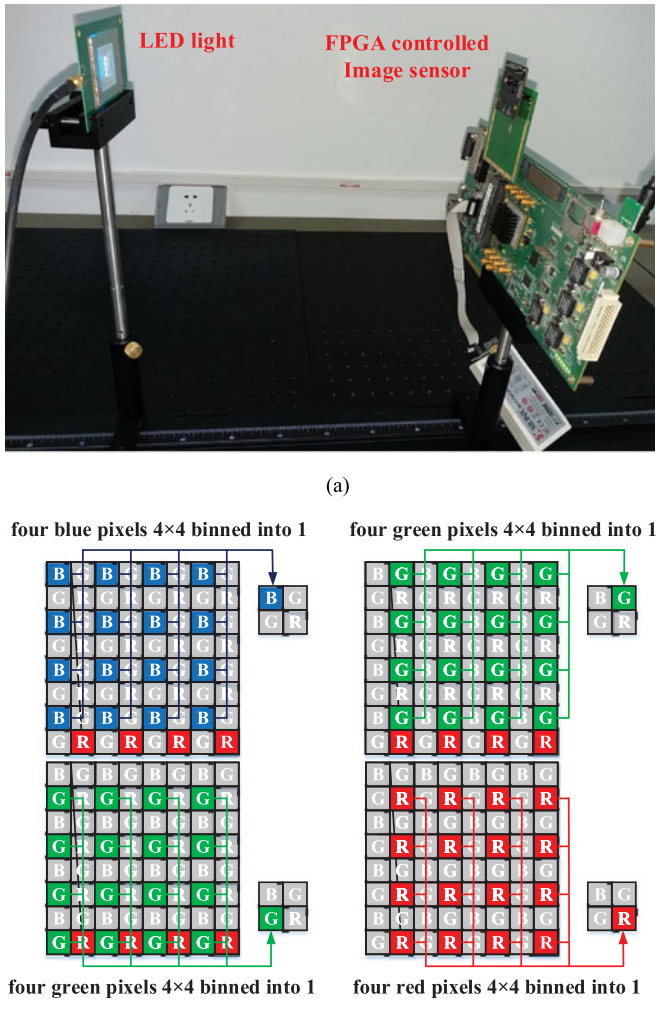

Fig. 4. Experimental setup and image sensor binning mode. (a) Experimental setup. (b) Illustration of 4×4 binning.

to estimate the noise characteristics. Due to the Bayer-pattern color filters layout in the deployed image sensor, each pixel produces signal components corresponding to the red/green/blue colors respectively. Thus, in the experiment we measured the noise distributions for the red/green/blue pixel components respectively. Fig. 4(a) shows the experimental setup. An LED light source is used as the transmitter and a field programmable gate array (FPGA) is employed to control the CMOS image sensor to capture the images with RAW format in a successive manner. Note that the image sensor used in the experiment is in the 4×4 binning mode as in Fig. 4(b), which means the noises are spatially averaged in the binning mode. Similarly averaging was performed in the corresponding simulation under the specified parameter setting. Fig. 5(a) shows the model-based simulation results and experimentally measured results about the noise distribution. The mean value $\mu = 240$ and the standard deviation $\sigma = 2.368$ were obtained by the maximum likelihood estimation of the Gaussian distribution parameters on 95% confidence intervals. It is observed that, the Gaussian distribution fits both simulation and measurement results very well. This indicates that the ISC noise can be modeled by a Gaussian distribution with very good accuracy.

Next, we examine how the Gaussian noise variance varies with the input and further validate our proposed M-SDGN model, and we investigate the relationship between input signal and output

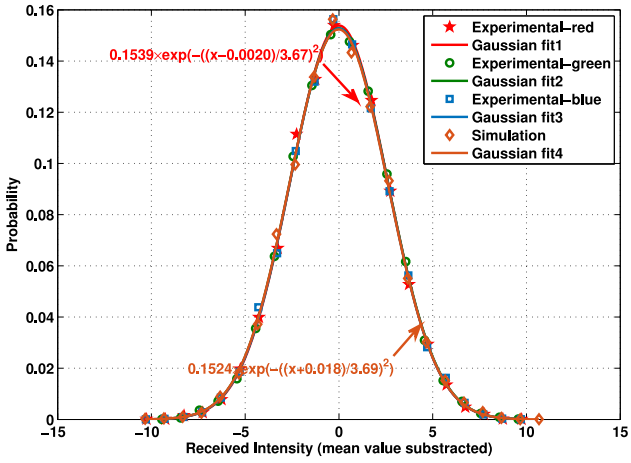

(a)

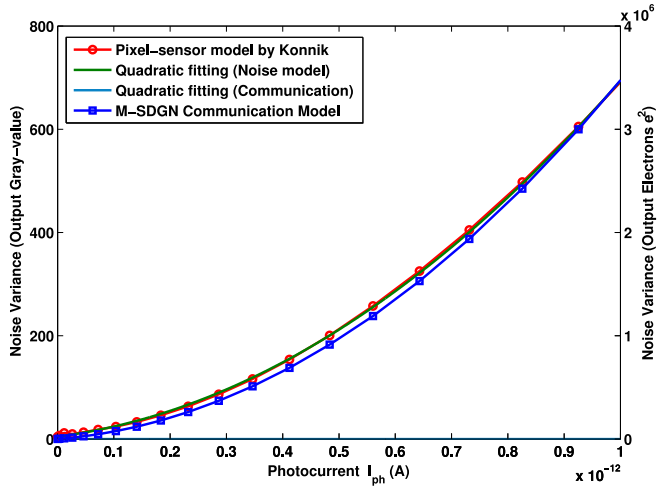

(b)

Fig. 5. Noise characteristics in OCC. (a) Probability density function of the noise based on experimental measurements (mean value $\mu = 240$ is subtracted). (b) Comparison of measured noise variances as a function of intensity with those from different fitting models.

noise variance based on the pixel-sensor model by Konnik [16], since this model can simulate realistic effects of noise on the images obtained from solid-state photosensors. Fig. 5(b) shows the variance of generated signal from 50 000 frame images as a function of the photocurrent I_{ph}, which is proportional to the transmitted light intensity under normal background illumination. The variance is observed to be a nonlinear function of photocurrent, and can be fit by a quadratic function with 95% confidence intervals. That means the output noise variance is a quadratic function of the input signal. The variance from simulation based on the model (14) is also presented for comparison. It can be fit by a quadratic function as well. These curves also agree with each other very well.

The dominance of different noise sources varies with operation conditions. Fig. 6(a) shows the ratio between the variance $\varsigma_1^2\sigma^2 X$ of signal-dependent shot noise $\sqrt{X}Z_1$ and variance σ^2 of generalized signal-independent noise Z_0, for different integration time, photocurrent and PRNU factor. According to the figure, $\varsigma_1^2 X$ is about $0.04 \sim 2$ when the photocurrent $I_{ph} = 10^{-15}A \sim 10^{-13}A$ under the general parameter setting. Similarly, Fig. 6(b) is for the signal-dependent PRNU noise

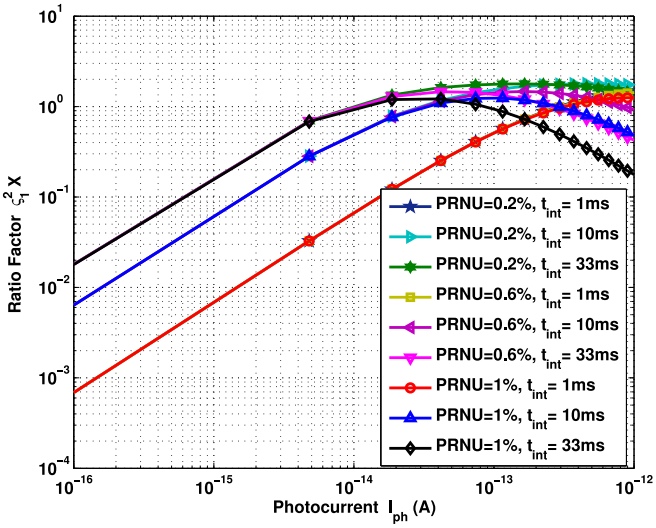

(a)

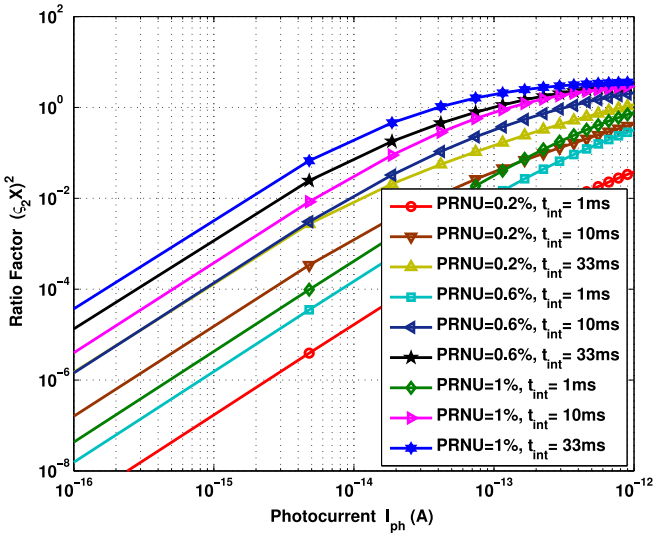

(b)

Fig. 6. Ratio between (a) signal-dependent shot noise power and generalized signal-independent noise power and (b) signal-dependent PRNU power and generalized signal-independent noise power.

XZ_2 with variance $\varsigma_2^2\sigma^2X^2$. We can see that $\varsigma_2^2X^2$ is about $10^{-7} \sim 2$ when the photocurrent $I_{ph} = 10^{-15}A \sim 10^{-13}$A.

4.2 SNR and Channel Capacity

The ISC system SNR depends on various factors. Fig. 7(a) shows SNR with different integration time. We set pixel area $P_A = 3.75\ \mu$m $\times$ $3.75\ \mu$m, and integral time $t_{int} = 33$ ms in simulation if they are not specified. It can be seen that SNR increases with the photocurrent I_{ph}. For small photocurrent, readout noise and dark current shot noise dominate, and SNR increases 20 dB as photocurrent increases 10 dB. As photocurrent increases, signal-induced shot noise starts to dominate, and SNR increases slowly by 10 dB as photocurrent increases 10 dB. Further increase of

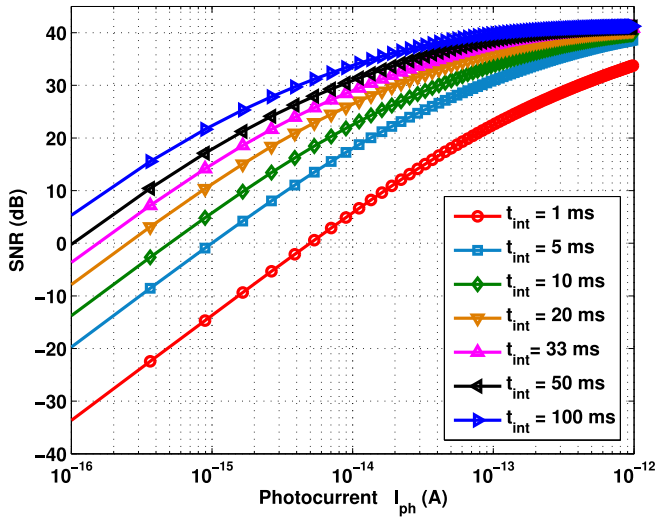

(a)

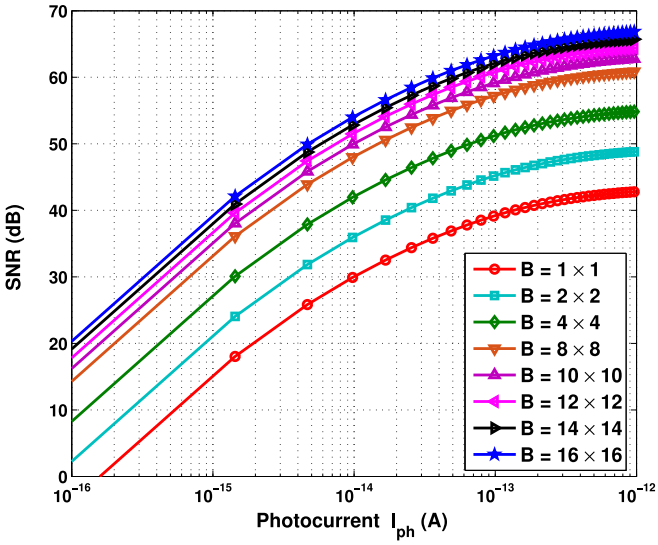

(b)

Fig. 7. SNR versus (a) photocurrent with different integration time and (b) different block size.

photocurrent leads to significant PRUN, and SNR flattens out. The achieved maximum SNR roughly approaches the well capacity before saturation. Most commercial CMOS image sensors provide frame rate exceeding 30 fps. For example, iPhone 7 supports 240 fps, and the frame rate of some special image sensor can even go beyond 1000 fps. According to this figure, SNR can range from 25 $\sim$ 38 dB under a general parameter setting, even when the frame rate exceeds 200 fps (short integration time).

To improve communication SNR, a potential solution is to leverage the spatial diversity of the sensor. Fig. 7(b) shows SNR with different pixel block size. It can be seen that SNR is roughly proportional to the block size in terms of the total number of pixels within the block for small to medium photocurrent. When the pixel block size is 2 $\times$ 2, 4 $\times$ 4 or 8 $\times$ 8, SNR in these blocks can be improved by about 6 dB, 12 dB and 18 dB as compared with 1 $\times$ 1 pixel block when photocurrent is between $10^{-16}A$ and $10^{-14}A$. The SNR is observed to be proportional to the number of pixels in

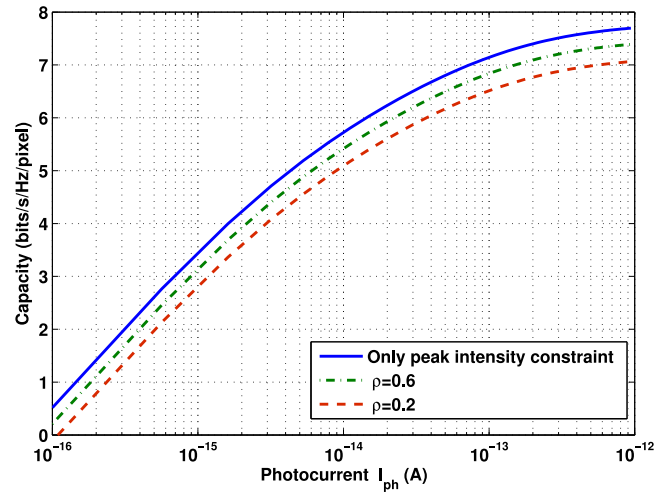

(a)

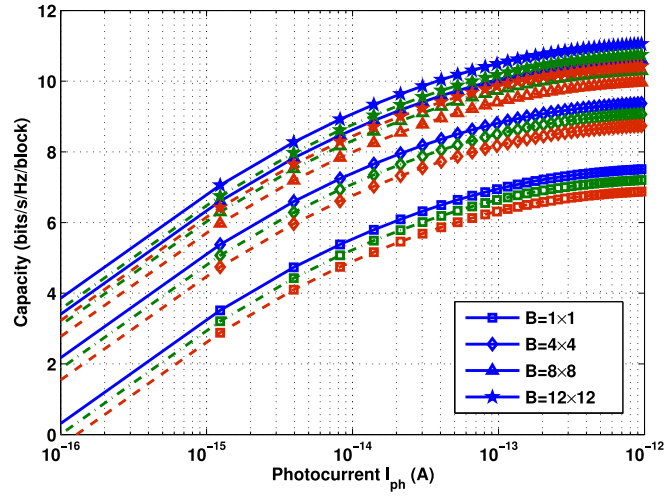

(b)

Fig. 8. Channel capacity (a) single-pixel receiver and (b) block-pixels receiver with different pixels block size under ideal channel. Blue line: only peak intensity constraint. Green dash dot line: $\rho = 0.6$. Fuchsia dash line: $\rho = 0.2$.

the block. The observation also holds for other cases as the block size continues to increase. This is due to noise reduction by spatial averaging and the block of the pixels serves as the receiver for the current single-input single-output (SISO) channel. If the sensor area is partitioned into blocks and each block serves as one receiver, the number of receivers decreases as the block size increases for a fixed sensing area. In such a case, the number of parallel sub-channels decreases if multiple LED sources are deployed, and the system capacity of the corresponding multiple-input multiple-output (MIMO) channel will be affected. The study of the MIMO channel capacity is beyond the scope of the current work and will be carried out in the future.

Based on the SNR and proposed channel model, we apply the search algorithm in [21] to find the input probability distribution maximizing the capacity, where a discrete input distribution of finite number of probability mass points can be numerically recorded. Then we obtain the channel capacity. Fig. 8(a) shows the capacity results for single-pixel receiver based ISC with peak and average-intensity constraints (different APPR ρ). It is observed that capacity increases with the

photocurrent or as ρ gets larger, especially when $\rho = 1$, which corresponds to the case with peak intensity constraint only. The channel can achieve 7.1 bit/s/Hz per pixel when photocurrent is $I_{ph} = 10^{-13}A$, corresponding to SNR of 37 dB according to Fig. 7(a). The channel capacity can be further improved by grouping multiple pixels into a block. Fig. 8(b) shows the capacity for block-pixel receiver with different size. About 10.5 bit/s/Hz per block is possible when block size is $B = 12 \times 12$ and photocurrent $I_{ph} = 10^{-13}A$. As the block size increases, the capacity improvement slows down.

V. Conclusion

This work investigates the fundamental noise characteristics and performance of the ISC system. Different from the noise in image processing, we model the noise from the communication perspective. It covers PRNU, photo shot noise, dark current shot noise, source follower noise, sense node reset noise, and quantization noise. The simulation and experimental results demonstrate that the ISC receiver noise is Gaussian, including electrical thermal noise, signal-dependent and signal-independent shot noise. We further study the system SNR and capacity under intensity constraints. We show that capacity is achieved by a discrete input distribution consisting of finite number of mass points. Numerical results indicate capacity of at least 7 bit/s/Hz per pixel is possible. Future work will look into roles of misalignment distortion, perspective distortion, electrical crosstalk due to charge diffusion in APS, optical crosstalk due to a diffraction limited optical subsystem, and the MIMO channel capacity.

Appendix A
Proof of Proposition 3.1

This proposition can be similarly proved as in [29]. The authors therein have proven that for a Gaussian channel with signal-dependent noise and amplitude-limited input, the mutual information function $I(F_X)$ is a continuous and concave function of the distribution F_X, and moreover, a weakly differentiable function over $\mathcal{F}_X$. In [29], the Gaussian channel with signal-dependent noise is modeled as $Y = X + N(X) + Z$, where X is the channel input with an amplitude constraint $|X| \leq A$, $N(X)$ is the signal-dependent noise, and Z is the signal-independent noise. In our ISC channel, the signal-dependent noise term $N(X)$ is specified as $(XZ_2 + \sqrt{X}Z_1)$, as in (14), and the channel input has an amplitude constraint $X \in [0, A]$. In the following, we only briefly state the important claims, observations, and steps of the proof.

To prove $I_{F_X}(X;Y)$ is a continuous function of F_X, we first prove the conditional probability density function $f_{Y|X}(y|x)$ is bounded and continuous as in [22]. Then, based on (23) and Remark 1 and by using *Dominated Convergence Theorem*, we can conclude that the function $H_{F_X}(Y)$ is continuous function of the distribution. The continuity of $E_{F_X}\left[\log(1 + \varsigma_2^2 x^2 + \varsigma_1^2 x)\right]$ is straightforward by applying the *Dominated Convergence Theorem* once more. Hence $I_{F_X}(X;Y)$ is a continuous function of $F_X(x)$ as well.

To prove $I_{F_X}(X;Y)$ is a concave function of F_X, we first define the input distribution $F_\theta = \theta F_1 + (1-\theta)F_2,\ \theta \in [0,1]$. Then we can prove $f_Y(y;F_\theta) = \theta f_Y(y;F_1) + (1-\theta)f_Y(y;F_2)$. Based on the boundedness of the entropy $|H_{F_X}(Y)|$, we can prove the output entropy corresponding to the input distribution F_θ satisfies $H_{F_\theta}(Y) \geq \theta H_{F_1}(Y) + (1-\theta)H_{F_2}(Y)$. Thus, $H_{F_X}(Y)$ is a concave function of F_X. For the mutual information, it can be easily proven that $I_{F_\theta = \theta F_1 + (1-\theta)F_2}(X;Y) \geq \theta I_{F_1}(X;Y) + (1-\theta)I_{F_2}(X;Y)$. Thus, $I_{F_X}(X;Y)$ is a concave function of the input distribution function.

To prove $I_{F_X}(X;Y)$ is weakly differentiable over $\mathcal{F}_X$, we define arbitrary input distribution $F_1, F_2 \in \mathcal{F}_X$, and consider the input distribution $F_\theta = \theta F_1 + (1-\theta)F_2$. Moreover, we define $J(\theta, F_1, F_2) = \frac{I_{F_\theta}(X;Y) - I_{F_1}(X;Y)}{\theta}$. By following the arguments in [19], we have $\lim_{\theta \to 0} \frac{H_{F_\theta}(Y) - H_{F_1}(Y)}{\theta} = \int_0^A h(x;F_1)dF_2(x) - H_{F_1}(Y)$. Thus, we can obtain $I'_{F_1,F_2}(X;Y) = \lim_{\theta \to 0} J(\theta, F_1, F_2) = \int_0^A i(x,F_1)dF_2 - I_{F_1}(X;Y)$. Similar to conditions in [19], we present the sufficient and necessary conditions on the optimal distribution

F_0 as

$$i(x, F_0) - I_{F_0}(X;Y) \leq 0, \ \forall x \in [0, A] \tag{34}$$

$$i(x, F_0) - I_{F_0}(X;Y) = 0, \ \forall x \in E_0, \tag{35}$$

where E_0 is the set of points of increase of F_0.

Appendix B
Proof of Proposition 3.2

The proof is based on contradiction arguments by assuming that the set E_0 has an infinite number of mass points. Since the set E_0 is bounded, we can use *Bolzano Weierstrass Theorem* to argue that the set E_0 has a limit point. Then, we can extend the entropy function to the complex and show its analyticity on an open connected set in the complex plane. By doing so, we can use the *Identity Theorem* to establish contradiction arguments that lead to the impossibility of the set E_0 to have infinite number of points.

We first define the extension of the noise variance function $\sigma^2(x) = (1 + \varsigma_2^2 x^2 + \varsigma_1^2 x)$ on the real line as

$$\sigma^2(x) = \begin{cases} 1 & \text{if } x \leq 0 \\ 1 + \varsigma_2^2 x^2 + \varsigma_1^2 x & \text{if } x \in [0, A] \\ 1 + \varsigma_2^2 A^2 + \varsigma_1^2 A & \text{if } x \geq A\,. \end{cases} \tag{36}$$

Then, the logarithm of the noise variance function $\log(\sigma^2(x))$ was extended to the entire complex plane $\mathbb{C}$ excluding the branch cuts Φ as $\log(\sigma^2(z))$, i.e.,

$$\sigma^2 \cdot \sigma^2(z) = \sigma_n^2(z) + \sigma^2 = \sigma_r^2 + j\sigma_i^2. \tag{37}$$

That is, $\forall z \in \mathbb{C}$, i.e., $z = a + jb$, $|\sigma^2(z)| \leq \infty$, $|\sigma_r^2| \leq \infty$, and $|\sigma_i^2| \leq \infty$.

The function $h(x; F_X)$ can also be extended to the complex plane $\mathbb{C}$, when $\forall z\ |z| < \infty$, due to the finiteness of $|h(z; F_x)|$ as in [20]. Then, we show that the marginal entropy $h(z; F_x)$ is an analytic function under some restrictions on the noise variance. Moreover, we also assume that the function $\log(\sigma^2(z))$ is analytic over some open connected set on the complex domain excluding some branch cuts.

Similar to [20, Prop. 3], we can invoke the *Dominated Convergence Theorem* to conclude the continuity of $h(z; F_X)$ for any domain $\mathcal{D}_\delta$ for an arbitrary $\delta > 0$, where $\mathcal{D}_\delta \triangleq \{z : |\text{Im}(z) \leq \delta|\}$. To show that the function $h(z; F_X)$ is analytic on the complex plane, it is sufficient to show that this function is analytic for any $z \in \mathbb{C}$ such that $|z| < \infty$. Because the function $\sigma^2(z)$ is analytic, then it is clear that the function $f_{Y|Z}(y|z)$ is analytic as well. Thus, by invoking *Morera's Theorem*, we have

$$\begin{aligned} \oint_\omega h(z; F_X)dz &= -\oint_\omega \int_{-\infty}^{\infty} f_{Y|Z}(y|z)\log(f_Y(y; Fx))dydz \\ &\overset{(a)}{=} \int_{-\infty}^{\infty} \log(f_Y(y; Fx)) \oint_\omega f_{Y|Z}(y|z)dydz = 0 \end{aligned} \tag{38}$$

where the order of integration in (a) is changed using *Fubini's Theorem*, and the reason we apply *Fubini's Theorem* is based on the finiteness of the whole integration, as [22, Lemma 5]. Thus, the function $h(z; F_X)$ is analytic on any domain $\mathcal{D}_\delta$, and is straightforward that $i_{F_X}(x)$ can be extended to the complex plane too.

Next we prove the discreteness of the optimal distribution. We first assume that the set E_0 contains infinite number of mass points in $[0, A]$. Then, based on *Bolzano-Weierstrass Theorem* [19], the set of these points admits a limit point. The marginal entropy function $h(z, F_X)$ and $I_{F_0}(X;Y) + \log(\sigma^2(z)) + D$ are analytic on some open connected set $\mathcal{D}$ in the complex plane $\mathbb{C}$ that includes the real line $\mathbb{R}$, except for the set of branch point Φ. Using the *Identity Theorem*, we conclude that the

following equality holds on the entire real line except the branch points of $\log(\sigma^2(z))$:

$$h_{F_0}(x) = I_{F_0}(X;Y) + \frac{1}{2}\log(\sigma^2(x)) + D, \quad \forall x \in \mathbb{R} - \Phi. \tag{39}$$

We will show that this argument leads to a contradiction when x is sufficiently large.

We note that the branch points of the function $\log(\sigma^2(z))$ are only located in the region between $[0, A]$, because out of this region the noise variance is defined to be constant and strictly greater than 1 as in (36). To proceed, we adopt the same idea as in [20], [22]. Let us define $L \triangleq I_{F_0}(X;Y) + D + \frac{1}{2}\log(\sigma^2(A))$ and $\rho(y) \triangleq \log(f_Y(y;F_0)) + L + \frac{1}{2}\log(\sigma^2(A))$. Based on the definition of the constant L, for sufficiently large value of x, i.e., $x > A$, we have

$$\int_{-\infty}^{\infty} f_{Y|X}(y|x)\left[\log(f_Y(y;F_0)) - \frac{1}{2}\log(\sigma^2(A)) - D\right]dy = 0, \quad \forall x > A \tag{40}$$

where

$$f_{Y|X}(y|x) = \frac{e^{-\frac{(y-x)^2}{2\pi\sigma^2(1+\varsigma_2^2A^2+\varsigma_1^2A)}}}{\sqrt{2\pi\sigma^2(1+\varsigma_2^2A^2+\varsigma_1^2A)}}, \quad \forall x > A. \tag{41}$$

Define

$$\Omega^+ \triangleq \{y : \rho(y) \geq 0\}, \quad \Omega^- \triangleq \{y : \rho(y) < 0\}. \tag{42}$$

Then

$$\int_{\Omega^+} f_{Y|X}(y|x)\rho(y)dy + \int_{\Omega^-} f_{Y|X}(y|x)\rho(y)dy = 0. \tag{43}$$

By (20), we get $\rho(y) \leq \log(\Gamma(y)) + L + \frac{1}{2}\log(\sigma^2(A)) \leq \log(k_3) + L + \frac{1}{2}\log(\sigma^2(A))$ for any $y \in \mathbb{R}$, and $x > A$. Hence, equation (43) requires $k_3 > 2^{-(L+\frac{1}{2}\log(\sigma^2(A)))}$. Choose a constant l such that $l > A - \frac{1}{\pi k_3^2}\log(k_3)$. Using (20), one has $\Omega^+ \subseteq [-l, l]$. Therefore

$$\begin{aligned}
&\int_{\Omega^+} f_{Y|X}(y|x)\rho(y)dy \leq \int_{-l}^{l} f_{Y|X}(y|x)\rho(y)dy \\
&\leq \left(\log(k_3) + L + \frac{1}{2}\log(\sigma^2(A))\right)\int_{-l}^{-l} f_{Y|X}(y|x)dy \\
&\leq \left(\log(k_3) + L + \frac{1}{2}\log(\sigma^2(A))\right) \times 2l\Gamma(x-l).
\end{aligned} \tag{44}$$

We can make this upper bound arbitrarily small by choosing x large enough due to the monotonicity of $\Gamma(\cdot)$. On the other hand, for $x > A + l$

$$\begin{aligned}
&\int_{\Omega^-} f_{Y|X}(y|x)\rho(y)dy \leq \int_{l}^{\infty} f_{Y|X}(y|x)\rho(y)dy \\
&\leq \int_{l}^{\infty} f_{Y|X}(y|x)\left[\log(\Gamma(y)) + L + \frac{1}{2}\log(\sigma^2(A))\right]dy \\
&\overset{(a)}{\leq} \frac{1}{2}\log(\Gamma(y-A)) + L + \frac{1}{2}\log(\sigma^2(A)) < 0
\end{aligned} \tag{45}$$

where (a) follows from both (21) and the fact that the integrable function is monotone in y. By combining (44) and (45), (43) cannot hold for sufficiently large x. Hence, there is contradiction and the set E_0 cannot have an infinite number of mass points. Thus, the number of mass point of F_0 must be finite.

References

[1] "Image sensors market analysis," 2016. [Online]. Available: http://www.grandviewresearch.com/industry-analysis/imagesensors-market

[2] P. H. Pathak, X. Feng, P. Hu, and P. Mohapatra, "Visible light communication, networking, and sensing: A survey, potential and challenges," *IEEE Commun. Surv. Tuts.*, vol. 17, no. 4, pp. 2047–2077, Oct.–Dec. 2015.

[3] N. Saha, M. S. Ifthekhar, N. T. Le, and Y. M. Jang, "Survey on optical camera communications: challenges and opportunities," *IET Optoelectron.*, vol. 9, no. 5, pp. 172–183, 2015.

[4] T. Yamazato *et al.*, "Image-sensor-based visible light communication for automotive applications," *IEEE Commun. Mag.*, vol. 52, no. 7, pp. 88–97, Jul. 2014.

[5] T. Li, C. An, A. T. Campbell, and X. Zhou, "Highlight: Hiding bits in pixel translucency changes," *ACM SIGMOBILE Mobile Comput. Commun. Rev.*, vol. 18, no. 3, pp. 62–70, 2015.

[6] Y.-S. Kuo, P. Pannuto, K.-J. Hsiao, and P. Dutta, "Luxapose: Indoor positioning with mobile phones and visible light," in *Proc. 20th Annu. Int. Conf. Mobile Comput. Netw.*, 2014, pp. 447–458.

[7] "The ieee 802.15.7r1 study group," 2015. [Online]. Available: http://www.ieee802.org/15/pub/IEEE%20802_15%20WPAN%2015_720Revision1%20Task%20Group.htm

[8] "The IEEE 802.15 documents," [Online]. Available: https://mentor.ieee.org/802.15/documents

[9] W. Hu, H. Gu, and Q. Pu, "Lightsync: unsynchronized visual communication over screen-camera links," in *Proc. 19th Annu. Int. Conf. Mobile Comput. Netw.*, 2013, pp. 15–26.

[10] W. Huang, P. Tian, and Z. Xu, "Design and implementation of a real-time CIM-MIMO optical camera communication system," *Opt. Exp.*, vol. 24, no. 21, pp. 24 567–24 579, 2016.

[11] S. Hranilovic and F. R. Kschischang, "A pixelated MIMO wireless optical communication system," *IEEE J. Sel. Top. Quantum Electron.*, vol. 12, no. 4, pp. 859–874, Jul./Aug. 2006.

[12] T. Yamazato *et al.*, "Vehicle motion and pixel illumination modeling for image sensor based visible light communication," *IEEE J. Sel. Areas Commun.*, vol. 33, no. 9, pp. 1793–1805, Sep. 2015.

[13] A. El Gamal and H. Eltoukhy, "CMOS image sensors," *IEEE Circuits Devices Mag.*, vol. 21, no. 3, pp. 6–20, May/Jun. 2005.

[14] H. Tian, B. Fowler, and A. E. Gamal, "Analysis of temporal noise in CMOS photodiode active pixel sensor," *IEEE J. Solid-State Circuits*, vol. 36, no. 1, pp. 92–101, Jan. 2001.

[15] C.-R. Moon, J. Jung, D.-W. Kwon, J. Yoo, D.-H. Lee, and K. Kim, "Application of plasma-doping (PLAD) technique to reduce dark current of CMOS image sensors," *IEEE Electron Device Lett.*, vol. 28, no. 2, pp. 114–116, Feb. 2007.

[16] M. Konnik and J. Welsh, "High-level numerical simulations of noise in CCD and CMOS photosensors: Review and tutorial," arXiv preprint arXiv:1412.4031, 2014.

[17] A. J. Theuwissen, "CMOS image sensors: State-of-the-art," *Solid-State Electron.*, vol. 52, no. 9, pp. 1401–1406, 2008.

[18] R. D. Gow *et al.*, "A comprehensive tool for modeling CMOS image-sensor-noise performance," *IEEE Trans. Electron Devices*, vol. 54, no. 6, pp. 1321–1329, Jun. 2007.

[19] J. G. Smith, "The information capacity of amplitude-and variance-constrained scalar Gaussian channels," *Inf. Control*, vol. 18, no. 3, pp. 203–219, 1971.

[20] A. Tchamkerten, "On the discreteness of capacity-achieving distributions," *IEEE Trans. Inf. Theory*, vol. 50, no. 11, pp. 2773–2778, Nov. 2004.

[21] T. H. Chan, S. Hranilovic, and F. R. Kschischang, "Capacity-achieving probability measure for conditionally Gaussian channels with bounded inputs," *IEEE Trans. Inf. Theory*, vol. 51, no. 6, pp. 2073–2088, Jun. 2005.

[22] B. Mamandipoor, K. Moshksar, and A. K. Khandani, "On the sum-capacity of Gaussian MAC with peak constraint," in *Proc. IEEE Int. Symp. Inf. Theory Proc.*, 2012, pp. 26–30.

[23] R. M. Gagliardi and S. Karp, "Optical communications," New York, NY, USA: Wiley-Interscience, 1976. 445 p., vol. 1, 1976.

[24] A. A. Farid and S. Hranilovic, "Capacity bounds for wireless optical intensity channels with Gaussian noise," *IEEE Trans. Inf. Theory*, vol. 56, no. 12, pp. 6066–6077, Dec. 2010.

[25] G. K. Froehlich, "Estimation in signal-dependent noise," Ph.D. dissertation, Texas Tech Univ., Lubbock, TX, USA, 1980.

[26] S. M. Moser, "Capacity results of an optical intensity channel with input-dependent Gaussian noise," *IEEE Trans. Inf. Theory*, vol. 58, no. 1, pp. 207–223, Jan. 2012.

[27] S. Lang, *Complex Analysis*. Berlin, Germany: Springer, 2013, vol. 103.

[28] J. G. Smith, *On the Information Capacity of Peak and Average Power Constrained Gaussian Channels*. San Diego, CA, USA: Univ. Calif. Press, 1969.

[29] A. ElMoslimany, "A new communication scheme implying amplitude limited inputs and signal dependent noise: System design, information theoretic analysis and channel coding," Ph.D. dissertation, Arizona State Univ., Tempe, AZ, USA, 2015.